The Astrophysical Journal, 727:17 (14pp), 2011 January 20 doi:10.1088/0004-637X/727/1/17

NUMERICAL MODELING OF FOOTPOINT-DRIVEN MAGNETO-ACOUSTIC WAVE PROPAGATION IN A LOCALIZED SOLAR FLUX TUBE

V. Fedun[1], S. Shelyag[1,2], and R. Erdélyi[1]
[1] Solar Physics and Space Plasma Research Centre, Department of Applied Mathematics, University of Sheffield, Hounsfield Road, Hicks Building, Sheffield, S3 7RH, UK
[2] Astrophysics Research Centre, School of Mathematics and Physics, Queen's University Belfast, Belfast BT7 1NN, UK
Received 2010 August 17; accepted 2010 November 9; published 2010 December 23

ABSTRACT

In this paper, we present and discuss results of two-dimensional simulations of linear and nonlinear magneto-acoustic wave propagation through an open magnetic flux tube embedded in the solar atmosphere expanding from the photosphere through to the transition region and into the low corona. Our aim is to model and analyze the response of such a magnetic structure to vertical and horizontal periodic motions originating in the photosphere. To carry out the simulations, we employed our MHD code SAC (Sheffield Advanced Code). A combination of the VALIIIC and McWhirter solar atmospheres and coronal density profiles were used as the background equilibrium model in the simulations. Vertical and horizontal harmonic sources, located at the footpoint region of the open magnetic flux tube, are incorporated in the calculations, to excite oscillations in the domain of interest. To perform the analysis we have constructed a series of time–distance diagrams of the vertical and perpendicular components of the velocity with respect to the magnetic field lines at each height of the computational domain. These time–distance diagrams are subject to spatio-temporal Fourier transforms allowing us to build ω–k dispersion diagrams for all of the simulated regions in the solar atmosphere. This approach makes it possible to compute the phase speeds of waves propagating throughout the various regions of the solar atmosphere model. We demonstrate the transformation of linear slow and fast magneto-acoustic wave modes into nonlinear ones, i.e., shock waves, and also show that magneto-acoustic waves with a range of frequencies efficiently leak through the transition region into the solar corona. It is found that the waves interact with the transition region and excite horizontally propagating surface waves along the transition region for both types of drivers. Finally, we estimate the phase speed of the oscillations in the solar corona and compare it with the phase speed derived from observations.

Key words: magnetohydrodynamics (MHD) – shock waves – Sun: atmosphere – Sun: oscillations

Online-only material: color figures

1. INTRODUCTION

Magnetic field plays a fundamental role in the dynamical processes in the solar atmosphere. Magnetic structures connect the solar convection zone and photosphere through the transition region to the solar corona, and may act as a guide for the energy supply, leaking it from the solar interior to the outer atmosphere (see, e.g., De Pontieu et al. 2004, 2005) which is necessary for coronal heating.

Modern ground- and space-based observational instruments, e.g., ROSA, SST, CoMP, *SOHO*, *Hinode*/SOT, *SDO*/AIA allow us to study the radiation originating in the solar atmosphere. Numerous observations of the presence of MHD waves in the solar atmosphere have been reported (see, e.g., the reviews on waves and oscillations in open magnetic structures, Banerjee et al. 2007; on propagating magneto-acoustic waves, De Moortel 2009; on Alfvén waves, Mathioudakis et al. 2011; on the topic of leakage of *p*-modes into the transition region, De Pontieu & Erdélyi 2006 and others). The observational report by Scullion et al. (2010) claims to determine horizontally propagating energetic transition region quakes as a result of the wave leakage. Erdélyi & Taroyan (2008) has shown the detection of oscillations by the EUV Imaging Spectrometer (*Hinode*/EIS). There is no evidence that these motions are generated by a flare. This is an important indication for our current study and is the *Hinode* counterpart of observations by Tomczyk & McIntosh (2009).

A certain lack of the detailed understanding of the physical processes in the solar plasma often makes it difficult to unambiguously analyze the observations. The conditions of the plasma in the solar atmosphere are described reasonably well by the MHD equations. For a strongly stratified plasma with a non-uniform magnetic field configuration, the analytical solutions of the MHD equations are not known, thus, numerical simulations have to be used for such studies.

Theoretical investigations of wave propagation through the solar plasma attracted particular attention due to the possibility of inferring the detailed plasma properties from the observations of solar oscillations. This (known as helioseismological) technique has been considerably exploited to unveil the properties of the (invisible) solar interior. Only recently, with the advent of observational instruments with particularly high spatial and temporal resolutions, has this seismological approach been generalized to the solar chromosphere and corona (see, e.g., Erdélyi 2006; Erdélyi & Fedun 2007; Andries et al. 2009; De Moortel 2009; Ruderman & Erdélyi 2009, for reviews with a range of applications).

A variety of one- and multi-dimensional HD and MHD numerical simulations of the solar atmosphere have already been performed. Recently, linear and nonlinear magneto-acoustic wave propagation through a magnetic flux tube has been studied numerically by Cargill et al. (1997), Bogdan et al. (2003), Hasan et al. (2005), Carlsson & Bogdan (2006), Khomenko & Collados (2006), Khomenko et al. (2008), Hasan & van Ballegooijen (2008), Taroyan & Erdélyi (2009), Ofman (2009), Fedun et al. (2009), and others. The properties of wave propagation in such numerical simulations, as in the real Sun, are highly sensitive to the properties of the background atmosphere and

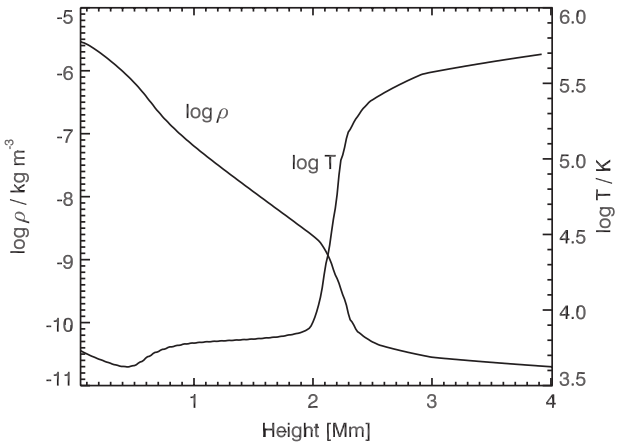

Figure 1. Vertical dependences of logarithms of the density ρ and the temperature T in the computational domain. These profiles are constructed using atmospheric parameters for the average quiet Sun (VAL IIIC; Vernazza et al. 1981) for the lower part of the model, and McWhirter et al. (1975) coronal model for the upper (corona) region.

the configuration of the magnetic field (as pointed out in various investigations by Díaz & Roberts 2006; Ruderman et al. 2008; Verth et al. 2008; Verth & Erdélyi 2008; Zaqarashvili & Skhirtladze 2008; Kuridze et al. 2009; Verth et al. 2010).

Cargill et al. (1997) examined the evolution of a nonlinear Alfvén wave pulse in the region between the solar photosphere and corona. The magnetic field was chosen to be potential and the background density and temperature were constructed analytically. These profiles lie somewhere between those expected in the quiet Sun and active regions. Bogdan et al. (2003) constructed a two-dimensional, time-dependent hydrostatic isothermal MHD model for the investigation of slow and fast magneto-acoustic-gravity monochromatic wave generation, propagation, transformation and interaction in the solar photosphere and chromosphere regions. The basic magnetic configuration consisted of a large unipolar magnetic flux concentration surrounded on each side by two smaller concentrations of opposite-polarity field. This type of magnetic structure is a popular model for sunspots, pores or even smaller magnetic flux tubes like magnetic bright points where the equilibrium magnetic field is strong.

A non-uniform and non-potential magnetic field configuration embedded in a non-uniform photospheric model has been investigated by Khomenko & Collados (2006) to study the processes taking place around the equipartition layer (where $V_A = C_S$) in sunspots.

As the magnetic building block of the lower solar atmosphere, the chromospheric magnetic network has been simulated by Hasan et al. (2005) and Hasan & van Ballegooijen (2008) as a thin (1000 km) layer of the solar atmosphere embedded in non-potential flux tube with periodic horizontal boundary conditions. These boundary conditions provide a limit in the simulations due to the fast waves generated in the system reaching the boundaries rather quickly.

It is now of particular interest, for the studies of solar MHD waves and oscillations, to extend the simulations to include the lower solar corona region, especially in light of their relevance to MHD heating of the solar corona and the available *SDO* data showing wave coupling from the chromosphere to the corona. Such an extension in the modelling represents significant difficulties for the actual implementation of simulations due to, e.g., the tremendous range of the thermodynamical parameters (and, correspondingly, sound speed) in the simulated region.

It should also be mentioned that in our simulations the radiative losses, dissipative and thermal conduction terms are not included. Importance of these effects on wave propagation and mode conversion will be analyzed in future.

In this work, the propagation of slow and fast magneto-acoustic waves, excited by vertical and horizontal drivers, in a two-dimensional magnetic flux tube embedded in a realistically stratified solar atmosphere from the photospheric region to the lower part of solar corona is addressed. We have analyzed the time–distance and spectral properties of wave propagation in the various solar atmospheric regions spanning from photosphere to corona.

The paper is organized as follows. The numerical method used to carry out the simulations and the model of the solar atmosphere are outlined in Section 2. The magnetic field configuration and the sources that generate the wave modes in the computational domain are presented in Section 3. In the following section, we discuss and examine in detail the various aspects of linear and nonlinear wave evolution in the lower and upper solar atmospheric regions. Section 5 is the conclusion.

2. NUMERICAL METHODS AND MODEL

The two-dimensional version of the Sheffield Advanced Code (SAC) is applied to carry out the simulations. The code is built on the basis of the Versatile Advection Code (VAC) by Tóth (1996), Tóth et al. (1998), Tóth (2000), and Keppens et al. (2003). SAC is the reconfigurable multi-dimensional ideal MHD solver which is designed to simulate the nonlinear interaction of an arbitrary perturbation with a gravitationally stratified background model, i.e., a model of the solar atmosphere, in magnetohydrostatic equilibrium. The code uses variable separation and hyperdiffusive and hyper-resistive terms (Stein & Nordlund 1998; Caunt & Korpi 2001; Vögler et al. 2005; Shelyag et al. 2008) to stabilize the solution against numerical instabilities and imperfections in the background model, caused by truncation errors. The main advantage of the implemented numerical technique is that it allows us to robustly simulate the macroscopic processes in a gravitationally stratified, magnetized plasma. A full description of the code, tests for various standard HD and MHD problems and the implemented numerical schemes are given in Shelyag et al. (2008).

For the purpose of this paper the chosen two-dimensional numerical domain consists of four adjoined parts: the solar photospheric region including the temperature minimum, the chromosphere, the transition region and the solar corona. The upper boundary of the domain is located well within the coronal layers. As an initial background model, two solar atmosphere models are joined: the VALIIIC quiet Sun model of Vernazza et al. (1981) is used to simulate the region between the lower part of the photosphere; the transition region, and the region above the transition region is based on the McWhirter et al. (1975) atmosphere model. Logarithms of the density and temperature profiles along the vertical direction z are shown in Figure 1.

The simulation domain with the equilibrium parameters is shown in Figure 3. The dependence of (1) the logarithm of the background pressure, $\log(P_0)$, (2) the temperature, T, and (3) the magnetic field components, B_{0x} and B_{0z}, as functions of height z and horizontal distance x of the equilibrium model are plotted in four panels of Figure 3, respectively. Note that only the central part of the numerical box is shown here in the figures. The full numerical box is 4 Mm wide and 4 Mm high, and is resolved on 400 × 1976 gridpoints, respectively. The

white contours represent the iso-plasma-β surfaces, labeled by their appropriate value of plasma-β. The orange lines are the equilibrium magnetic field lines in the figure and indicate the background field distribution in the computational domain. The method used to construct the structure of the open flux tube is explained in the next section. Horizontal dashed lines mark the approximate location of the different solar atmospheric levels, i.e., photosphere, chromosphere, TR and solar corona. In all the present simulations we employ non-reflective ("open") boundary conditions for perturbed variables. This type of boundary conditions allows the linear and nonlinear waves to propagate through the domain boundaries without noticeable reflection or distortion.

3. THE MAGNETIC FIELD CONFIGURATION AND DRIVER

The well known self-similarity approach is used to construct the background non-potential magnetic field configuration. The main advantages of such type of magnetic field are the following. Self-similar magnetic fields have a rather simple analytical description. Compared to potential fields, the non-potential localized magnetic field configuration, which we use here, demonstrates a closer resemblance to intergranular magnetic field concentrations, observed in the solar photosphere, and to magnetic fields generated by dynamical simulations of magneto-convection (see, e.g., Shelyag et al. 2010). Finally, self-similar magnetic fields can be created with a lower expansion factor compared to their counterparts with potential fields, thus it is not necessary to use additional localized magnetic field structures or less-natural periodic boundaries to prevent the field describing a less realistic expansion. Following the self-similarity description, the open magnetic flux tube configuration is obtained analytically from the following set of equations:

$$B_{\rm x} = -\frac{\partial f}{\partial z} \cdot G\,(f)\,,$$

$$B_{\rm z} = \frac{\partial f}{\partial x} \cdot G\,(f)\,,$$

and

$$f = x \cdot B_{0\rm z},$$

where $B_{0\rm z}$ is the vertical z-component of the background magnetic field along the symmetry axis, and G is an arbitrarily chosen function which describes the horizontal profile (in two-dimensional cartesian geometry) of the vertical magnetic field component. In the present case this function is chosen to be

$$G\,(f) = A \cdot \exp\left(-\frac{f}{f_0}\right)^2,$$

where f_0 is the so-called opening factor of the magnetic flux tube. It should be noted that the magnetic field structure, designed by the approach outlined above, is divergence-free by definition. This is a very important practical advantage for numerical studies, where keeping $\nabla \cdot \mathbf{B}$ is a challenging task, see, e.g., Tóth et al. (1998) and Tóth (2000). The corresponding density and gas pressure deviations from their non-magnetic equilibrium counterparts in the domain are calculated by assuming the magneto-hydrostatic equilibrium condition, i.e.,

$$(\mathbf{B} \cdot \nabla)\,\mathbf{B} + \nabla\left(\frac{\mathbf{B}^2}{2}\right) + \nabla p = \rho \mathbf{g},$$

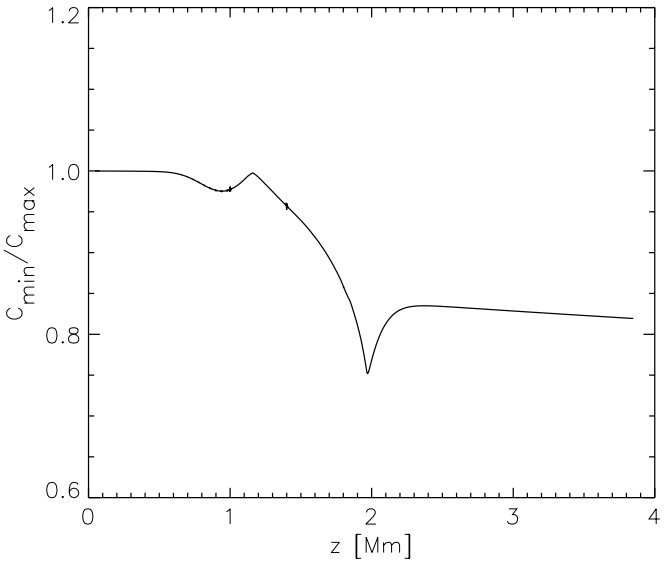

Figure 2. Vertical dependence of the ratio of the minimum to the maximum values of the sound speed taken along the cross section in the x-direction in the computational domain.

where p is the background kinetic pressure, g is the solar gravitational acceleration and ρ is the background density. This method was used previously by Schlüter & Temesváry (1958), Deinzer (1965), Schüssler & Rempel (2005), Gordovskyy & Jain (2007), Shelyag et al. (2009), and others. The strength of the magnetic field at the footpoint region is $B_0 = 45$ G. We are aware of the strength of present magnetic field is perhaps too low but it does make it possible to construct the flux tube without a strong opening at the solar corona region and thus makes it more practical to connect all four regions of the solar atmosphere. Low magnetic field strength is chosen not only for practical reasons. Full convective simulations of solar photosphere show that the intergranular lanes in the models of quiet solar granulation (with average unipolar magnetic flux 50 G) are full of vertical magnetic fields which rarely reach kilogauss values and normally stay within 100G limit. Thus, the chosen 45 G magnetic field represents quiet intergranular magnetic field concentrations quite reasonably. A stronger magnetic field is obviously interesting to analyze due to its connection to various visible features in the solar photosphere. An enhanced magnetic field would result in a downward shift of the equipartition layer and in a stronger opening of the magnetic flux tube, if the side boundaries of the domain are not periodic (which we obviously want to avoid, since the main point of the study is a single flux tube). Nevertheless, the chosen magnetic field strength is certainly a good approximation for weak and most likely ubiquitous solar flux tubes in the quiet Sun.

In Figure 2, we show the ratio of the minimum to the maximum values of the sound speed ($C_{\rm min}/C_{\rm max}$) taken at each height in the computational domain as a function of z. This plot allows us to clearly gain insight into the influence of the constructed magnetic flux tube on the background model. In the photosphere and lower chromospheric region $C_{\rm min}/C_{\rm max}$ is equal to unity. In the upper part of the chromosphere this ratio ($C_{\rm min}/C_{\rm max}$) is decreasing strongly, due to the increase of magnetic pressure inside the flux tube. In the transition region the influence of the magnetic field has maximum effect, which is evidenced in Figure 2 as a peak at $z = 1.95$ Mm. In the coronal region, the ratio $C_{\rm min}/C_{\rm max}$ has an approximately constant value of 0.82, i.e., the magnetic flux has a constant shape in this region.

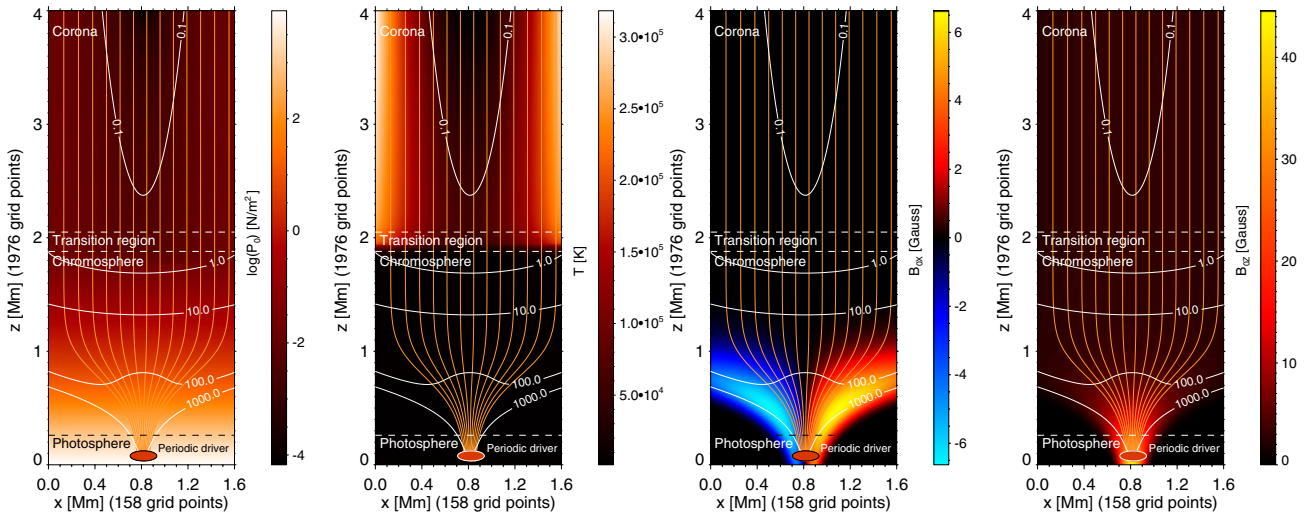

Figure 3. Initial state of the computational configuration. The logarithm of the background pressure, $\log(P_0)$ (a), the temperature, T (b), the magnetic field components, B_{0x} (c) and B_{0z} (d) are shown. The z-axis corresponds to altitude and the x horizontal axis is parallel to the solar surface. The orange lines visualize the magnetic field structure of the flux tube. The white lines are the iso-plasma-β contours, labeled by their values. The photosphere, chromosphere, transition region, and corona levels are highlighted schematically in the plot. Also, the position of the periodic driver (red ellipse) is illustrated at the footpoint region.

(A color version of this figure is available in the online journal.)

The driver is located at the footpoint region inside the flux tube just under the height corresponding to the temperature minimum of the solar atmosphere. The location is shown schematically in Figure 3 as a small red ellipse. In all the simulations for this study we have used a periodic driver with the frequency 33.3 mHz (or, equivalently, with the period of $\Delta t = 30$ s), similar to acoustic sources used by Bogdan et al. (2003), Hasan & van Ballegooijen (2008), and Fedun et al. (2009). Theory predicts (e.g., Musielak et al. 1994) a massive generation of high-frequency acoustic waves in the sub-photospheric region of the Sun, but, according to observational and numerical (one-dimensional) results of e.g., Fossum & Carlsson (2005), the acoustic energy flux created by these waves is too low to contribute in a dominant way to solar heating. Nevertheless, the generation of these high-frequency waves is not yet settled and additional studies are needed. High-frequency harmonic vertical and horizontal velocity drivers allow us to simulate wave coupling of the photosphere and corona. Further, analysis of these type of waves can be exploited for diagnostic purposes giving a unique opportunity for insight into sub-resolution properties of the solar wave guides. The V_x and V_z components of the velocity perturbation have Gaussian spatial profiles in the x and z directions,

$$V_{x,z} = A \sin\left(\frac{2\pi t}{\Delta t}\right) \exp^{-\left(\left(\frac{x-x_0}{\Delta x}\right)^2 + \left(\frac{z-z_0}{\Delta z}\right)^2\right)}, \qquad (1)$$

where A is the amplitude of the driver, x_0 and z_0 are the positions of the source center in the x and z directions, respectively.

4. SIMULATIONS

In our two-dimensional numerical simulations, as it was described previously, we implemented rather realistic density and temperature profiles. With such complicated flux tube structures it is not easy to identify the different types of propagating waves. Thus, we work with the velocity components perpendicular ($V_\perp$) and parallel ($V_\parallel$) to the background magnetic field instead of the velocity components defined in the Cartesian geometry. We suggest that the $V_\parallel$ component of the velocity corresponds mainly to the slow magneto-acoustic waves (SMAWs) and the $V_\perp$ component of the velocity corresponds to the fast magneto-acoustic waves (FMAWs). Of course, due to the strong decrease of the equilibrium density (see Figure 3), the sound speed changes with height dramatically and modes may interchange their character. In addition to that, the implemented magnetic structure imposes a change in the equilibrium density in both x and z directions. This latter feature results in additional changes to the sound speed in both the vertical and the horizontal directions. The local phase speeds for slow and fast MAWs also depend on the angle between the direction of the wave propagation and the magnetic field lines. According to MHD wave theory (see the recent, excellent textbook by Goedbloed & Poedts 2004), within the high plasma-β region ($C_S > V_A$), SMAWs propagate mainly along magnetic field lines with the local Alfvén speed V_A. The FMAW is allowed to propagate in any direction. Along the direction of field lines the FMAW travels with the sound speed C_S and in the direction perpendicular to the field lines it propagates with the phase speed $V_{ph} = \sqrt{(C_S^2 + V_A^2)}$.

On the other hand, within the region where the plasma-β is low ($V_A > C_S$), the MHD slow wave propagates approximately with the local sound speed C_S and the fast wave propagates with the local Alfvén speed V_A along the magnetic field lines. The angular dependence for the phase speeds of the slow and fast MAWs are identical in the high plasma-β region. Slow waves are prohibited from traveling perpendicularly to the magnetic field lines for both, high and low plasma-β regions. These well known defining features are recalled in order to help us to interpret the numerical results. Of course, in a structured and strongly inhomogeneous (e.g., stratified) magnetized plasma the modes are much harder to identify. They may be coupled to each other, or may transform from one mode to another while traveling through the medium.

In this paper, we analyze waves generated by the vertical and horizontal drivers in particular regions of the solar atmosphere that are side by side. We choose this principle of the presentation to make it easier to compare the interaction of the oscillations generated by these sources with the different regions of solar atmosphere.

The time evolution of parallel ($V_\parallel$) and transverse ($V_\perp$) components of the velocity produced by the vertical periodic

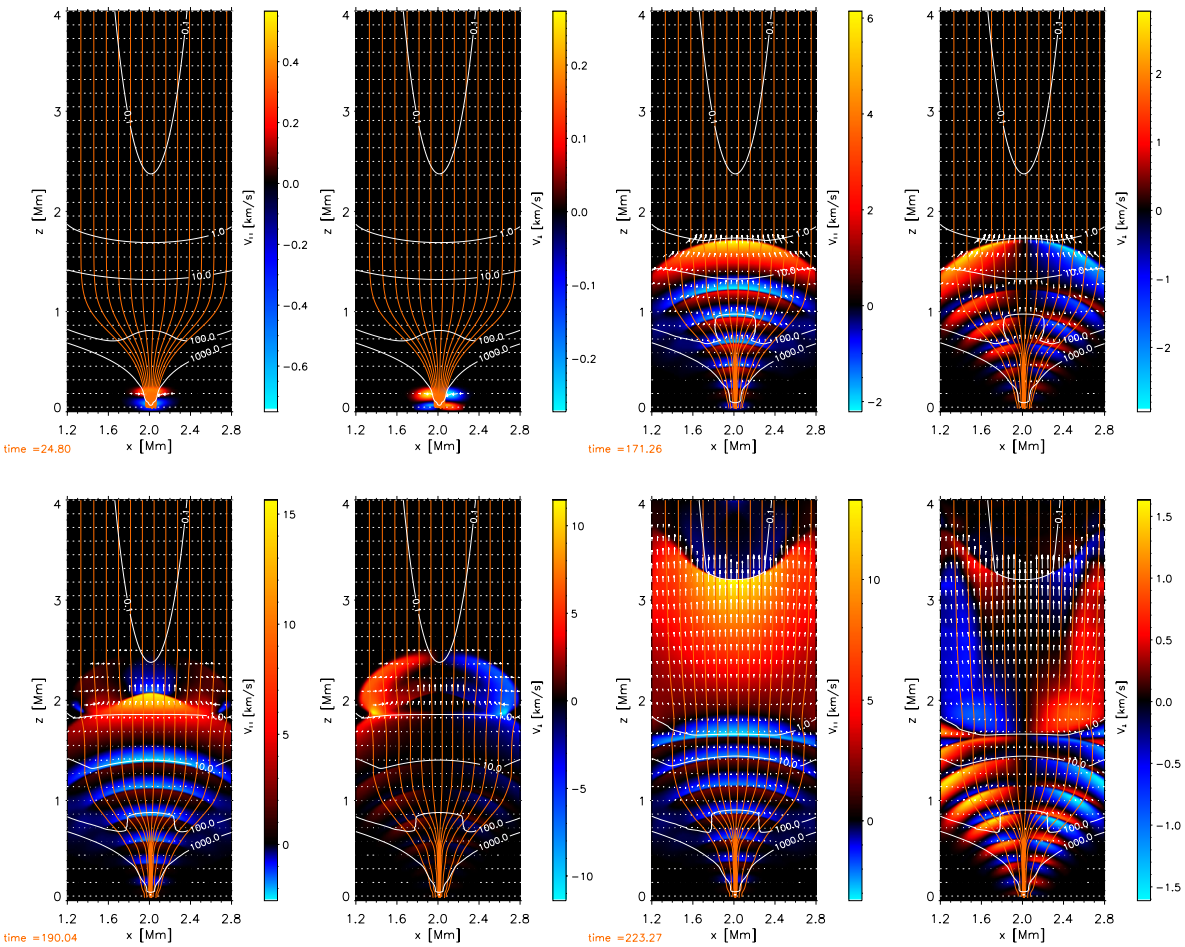

Figure 4. Snapshots of the field-aligned ($V_\parallel$) and transverse ($V_\perp$) components of the velocity response showing the temporal development of the initial perturbation generated by 30 s vertical periodic driver at different times in the open magnetic flux tube. The color scale shows the $V_\parallel$ and $V_\perp$ perturbations in km s^{-1} at times given in the bottom left corner of each pair of images. The color curves (i.e., white and orange) are same as on Figure 3. The angle and length of the white arrows correspond to the velocity vector field.

(A color version of this figure is available in the online journal.)

driver, specified by Equation (1), with amplitude $A = 500\,\mathrm{m\,s^{-1}}$, is shown in Figure 4. Illustrative snapshots are captured at times $t = 24$, 171, 190, and 223 s, respectively. Note that we will also use these time moments to show the simulation results with the horizontal driver (see Figure 6).

In the high plasma-β region, where the sound speed is greater than the Alfvén speed ($C_S \gg V_A$), e.g., applicable in photospheric and lower chromospheric regions, the generated waves propagate linearly and isotropically with an increase in amplitude due to the approximately constant sound speed C_S at the lower part of the computational domain (see two upper panels of Figures 4 and 5). It is clear that the waves are strongly acoustic in their character.

Next, we observe a very similar behavior of wave propagation at the lower part of the computational domain for waves excited by the horizontal periodic source (see Figures 6 and 7). It is virtually impossible to distinguish between the slow and fast waves at their initial stage in both types of simulation, as these waves are fully coupled. On the other hand, the vertical source of wave perturbations produces symmetric compressions and decompressions of the plasma inside the flux tube. The values of the relative pressure difference $\Delta P/P_0$ and temperature ΔT perturbations are shown in Figure 5. After this initial stage two waves (slow and fast), generated by vertical driver, can be observed in the simulation domain. As is evident from the snapshot taken at time $t = 170$ s (see upper right panel of Figure 4), in the region where the plasma-β is bounded within 10 (lower end) to 1.0 (upper end), the $V_\parallel$ and $V_\perp$ components of the velocity have different amplitudes and slightly different propagation angles.

The amplitude of $V_\parallel$ of the SMAW reaches approximately 6 km s^{-1} in the region below the TR from an initial value of 0.5 km s^{-1} in the photosphere while the $V_\perp$ amplitude of the FMAW grows to the smaller value of 2.8 km s^{-1}. Thus, the main part of wave energy produced by the vertical periodic driver is carried along the central part of the magnetic flux tube by the slow magneto-acoustic wave component. The FMAW is not observed along the axis of the magnetic flux tube. Since this latter wave propagates with a non-zero angle to the tube axis, it can be mainly detected at the edges of the flux tube. The propagation of the mainly longitudinal FMAW is visible as a symmetric motion of the magnetic field lines. In snapshots of the longitudinal $V_\parallel$ and the transversal $V_\perp$ velocity perturbations in Figure 4, it is apparent that the position of the magnetic field lines (highlighted as the orange lines in Figure 4) show symmetric expansions and contractions of the magnetic flux tube. This change of the magnetic flux tube diameter can be considered as an evidence of the sausage mode generated by the periodic vertical driver (see, e.g., Dorotovič et al. 2008), therefore we identify this

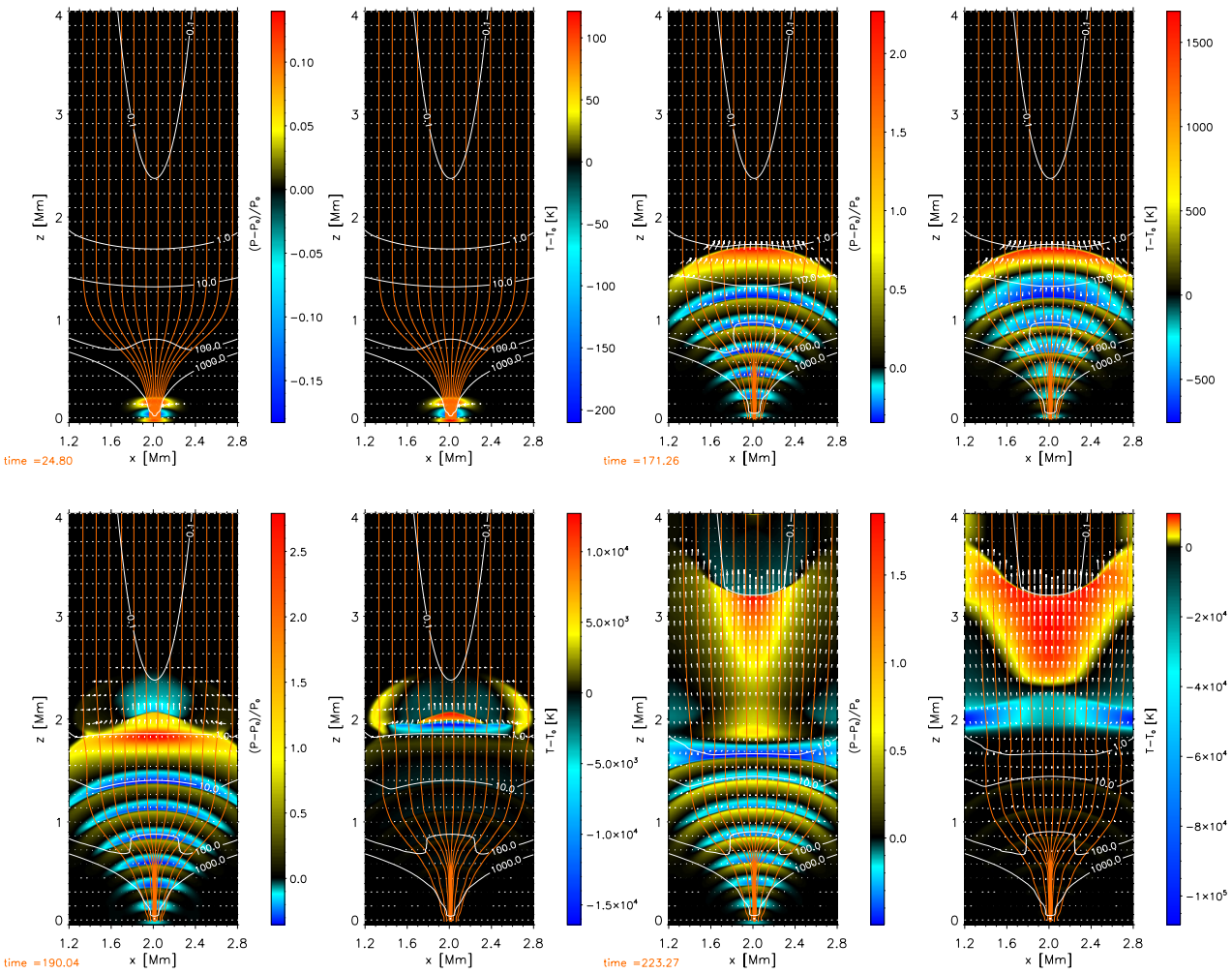

Figure 5. Snapshots of the relative pressure difference $\Delta P/P_0$ and temperature ΔT perturbation from the initial state in a magnetic flux tube at different times (same as Figure 3). The color scale shows the relative difference of pressure and temperature (in K) perturbations. The magnetic field lines and iso-plasma-β contours are the same as in Figure 3.

(A color version of this figure is available in the online journal.)

wave mode as a sausage wave guided by the magnetic flux tube structure.

Before analyzing our results regarding the horizontal driver, we should recall the recent paper by Goossens et al. (2009) on the nature of kink MHD waves in solar flux tubes. Goossens et al. (2009) have confirmed that in a magnetic flux tube, kink waves are incompressible waves with negligible pressure perturbations to a high degree of accuracy. In the central part of the open flux tube (see Figure 6), where the magnetic field is strong, we observe that the waves propagate upward with no noticeable gas or temperature perturbation (see Figure 7). We identify these perturbations to be the kink FMAW, since they have the same properties as described by Goossens et al. (2009). The amplitude of the initial perturbation of V_z (which in this particular case is equal to $V_\parallel$) increases from 0.5 km s^{-1} up to 2 km s^{-1}, and $V_\perp$ increases up to 0.7 km s^{-1} during the first few periods.

Therefore, similarly to the case of wave excitation by the vertical driver, the wave energy may be transferred to the upper part of solar atmosphere by longitudinal motions. This is an important point in regard to which type of wave modes generated by photospheric motions are most likely to supply energy for plasma heating in the upper part of the solar atmosphere.

In the upper part of the chromosphere, where the plasma-β is equal to or less than unity, all types of waves generated by both types of drivers (see Figures 4 and 6) have changed their character of propagation from linear to nonlinear. Hence, wave fronts become sharper and resemble shocks as they propagate upward into the region which has a stronger decrease in the background density profile. Due to different phase speeds of the waves, generated by the vertical and the horizontal drivers, as we pointed out previously, the time at which the wave perturbations penetrate and leak through the TR to the solar corona are different. The lower left panel of Figure 4 shows the moment of wave penetration into the solar corona ($t \cong 190$ s). On the right part of the panel, which depicts $V_\perp$, two shock-like structures are observed just above the TR. These shocks have similar circular shapes. On the left part of this panel ($V_\parallel$), at the axis of the magnetic flux tube, we can clearly see only one shock wave, which corresponds to the lower shock wave on the right part (i.e., $V_\perp$) of the panel. We suggest that the upper shock is related to FMAW mode and the lower shock is a SMAW. These two shocks have approximately the same maximum velocity values.

The slow magneto-acoustic shock wave propagates along the central part of the magnetic flux tube up to the coronal region. Opposite to that, the maximum amplitude of the fast magneto-acoustic (shock) wave is localized in the TR (see the lower left panel of Figure 4). Following this argument we

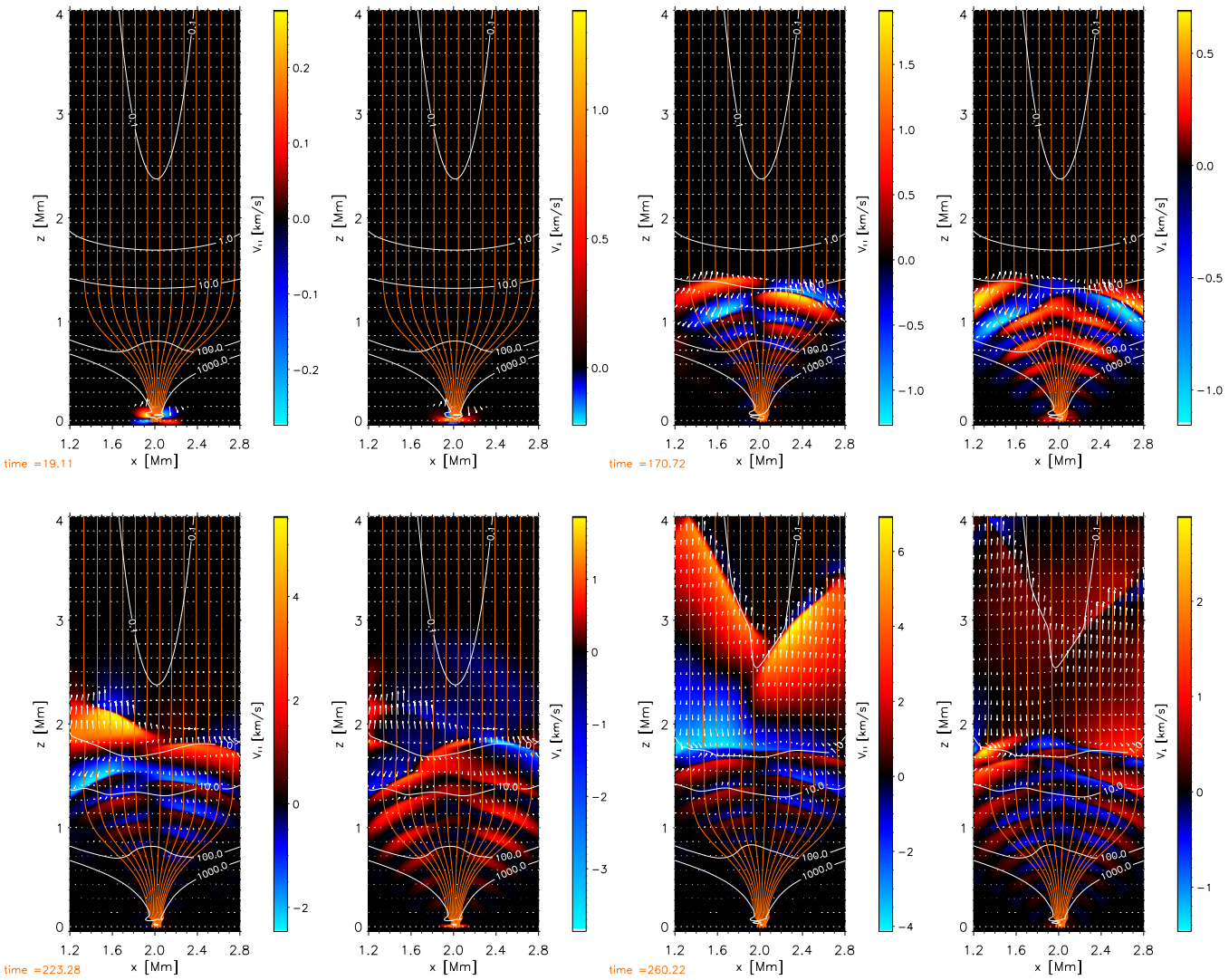

Figure 6. Same as Figure 4 but generated by 30 s periodic horizontal driver.
(A color version of this figure is available in the online journal.)

conclude that the main source of TR surface wave generation is the fast magneto-acoustic mode, i.e., generated by horizontal motions (see Figure 8). Note that in this figure only perturbations of the relative pressure difference ($\Delta P/P_0$) and temperature (ΔT), zoomed out for better visibility, at the TR region are shown.

In the lower right panel of Figure 6 we show the next stage of wave propagation and evolution, captured at a representative time of $t = 223$ s. The shock wave associated with the slow magneto-acoustic mode ($V_\parallel$) propagates upwards with an approximately constant shock amplitude of 15 km s^{-1}. The amplitude of this velocity component is about 10 times (i.e., an order of magnitude) greater than the amplitude of the transversal velocity component $V_\perp$. This feature has an important consequence for the energy propagation and supply to the solar corona.

Also, both slow and fast MAWs carry some part of their energy back to the photospheric region due to reflection from the TR (Schunker & Cally 2006; Fedun et al. 2009).

Due to the structure of the magnetic configuration under consideration, only the central part of the flux tube, where the magnetic field is strong (along the z-axis), can be used for comparison with the theory. Accordingly, as we have noted previously, the horizontal driver (Figure 6) generates fast kink MAWs at the central part of the tube. These type of waves can be identified by asymmetric motions of the magnetic field lines (orange lines in Figure 6) along the vertical, non-perturbed axis of the flux tube. The horizontal driver also generates symmetric, compressible motions (see Figure 7), similar to motions generated by the vertical driver, at the periphery of the magnetic flux tube. These latter waves are also FMAW, but do not displace the tube's axis. Such type of motion is visible in Figure 6 as a symmetric motion of the magnetic field lines (the orange lines). We appreciate that is difficult to identify the changes in magnetic field line positions in the static images. Therefore, to help readers, we also provided movies in a downloadable electronic format, that can be found at http://swat.group.shef.ac.uk. We also found that the largest portion of the wave energy is guided along the peripheral parts of the open magnetic flux tube, in contrast to the vertical driver case. In the coronal region, i.e., after penetration through the TR, the amplitude of the MHD waves, generated by the horizontal driver, reaches about 6.5 km s^{-1}. This value is two times less than in the case of the vertical driver.

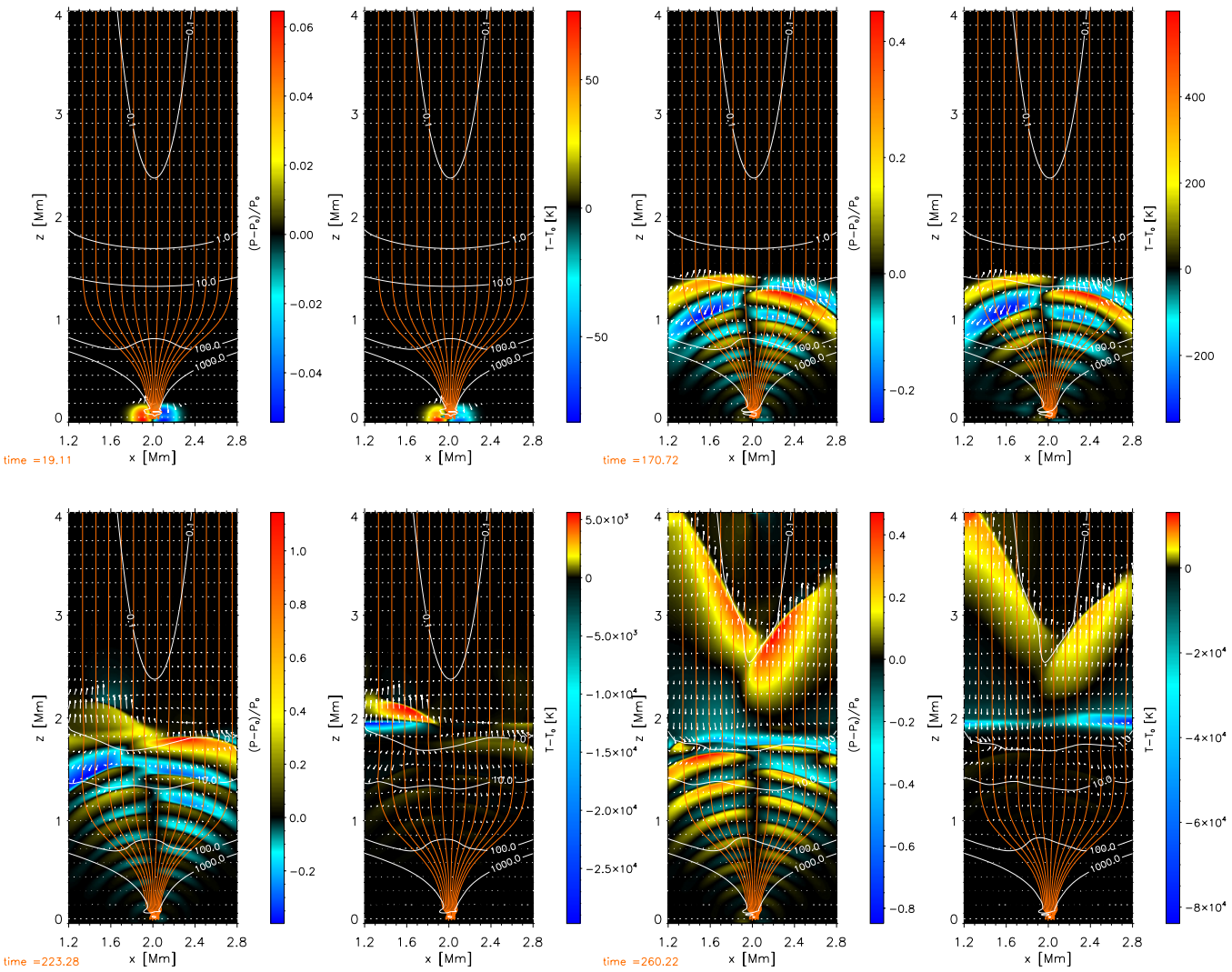

Figure 7. Relative pressure difference $\Delta P/P_0$ and temperature ΔT perturbation from the initial state in the magnetic flux tube at different times. Wave excitation is due to periodic horizontal motion. The color scale shows the relative difference of pressure and temperature perturbations. The colored (i.e., white and orange) curves are the same as in Figure 5.

(A color version of this figure is available in the online journal.)

Consequently, we can summarize that the energy is carried to the upper layers of the solar atmosphere mainly by the waves generated by vertical motions (see the lower right panel of Figure 6).

Also, similar to the generation of surface waves by the vertical driver, the horizontal motions at the photospheric region have a strong influence on surface wave excitation in the TR. To illustrate this, we have plotted a series of snapshots of relative pressure difference ($\Delta P/P_0$) and temperature (ΔT) perturbations at the TR at different representative times $t = 234$, 266, 288, and 317 s (see Figure 9).

The motions found in the TR have different features, i.e., they are symmetric to the axis of the open magnetic flux tube in the case of the vertical driver (see Figure 8), and they are asymmetric (see Figure 9) in the case of the horizontal driver. However, the amplitudes of the guided waves generated by the different types of sources are similar. The vertical ($V_\parallel$) and the horizontal ($V_\perp$) periodic motions produce variations of the temperature with amplitudes up to 150,000 K in this thin layer. These variations are approximately 10% of the temperature of the lower part of the solar corona and therefore can perhaps be detected by the currently available instruments.

To examine the dynamical processes in our simulations in greater detail, we have plotted time–distance diagrams of the parallel ($V_\parallel$) and the transverse ($V_\perp$) components of velocity. Figure 10 presents the simulation results in a different format. The time–distance diagrams are useful for relatively accurate measurements of the wave propagation speeds. As we have shown above, both types of the photospheric drivers generate the waves which, due to decoupling, can be resolved clearly only in the low plasma-β region.

The upper and lower panels of Figure 10 are plotted for the cases of vertical and horizontal driving sources, respectively. The thin white lines in these plots correspond to the constant plasma-β levels with the values of 100, 10, 1, and 0.1. We note, that these time–distance diagrams are taken at $x = 2.0$ Mm, i.e., along the axis of the open magnetic flux tube.

During the first three driving periods, i.e., within the first 90 s of the simulation, the vertical and horizontal harmonic sources produce linear waves, which propagate with an approximately constant speed of 11 km s^{-1}. After that, the steepness of the wavefront starts increasing due to the background stratification of the model. The changes of the constant plasma-β contour shapes are observed in the upper

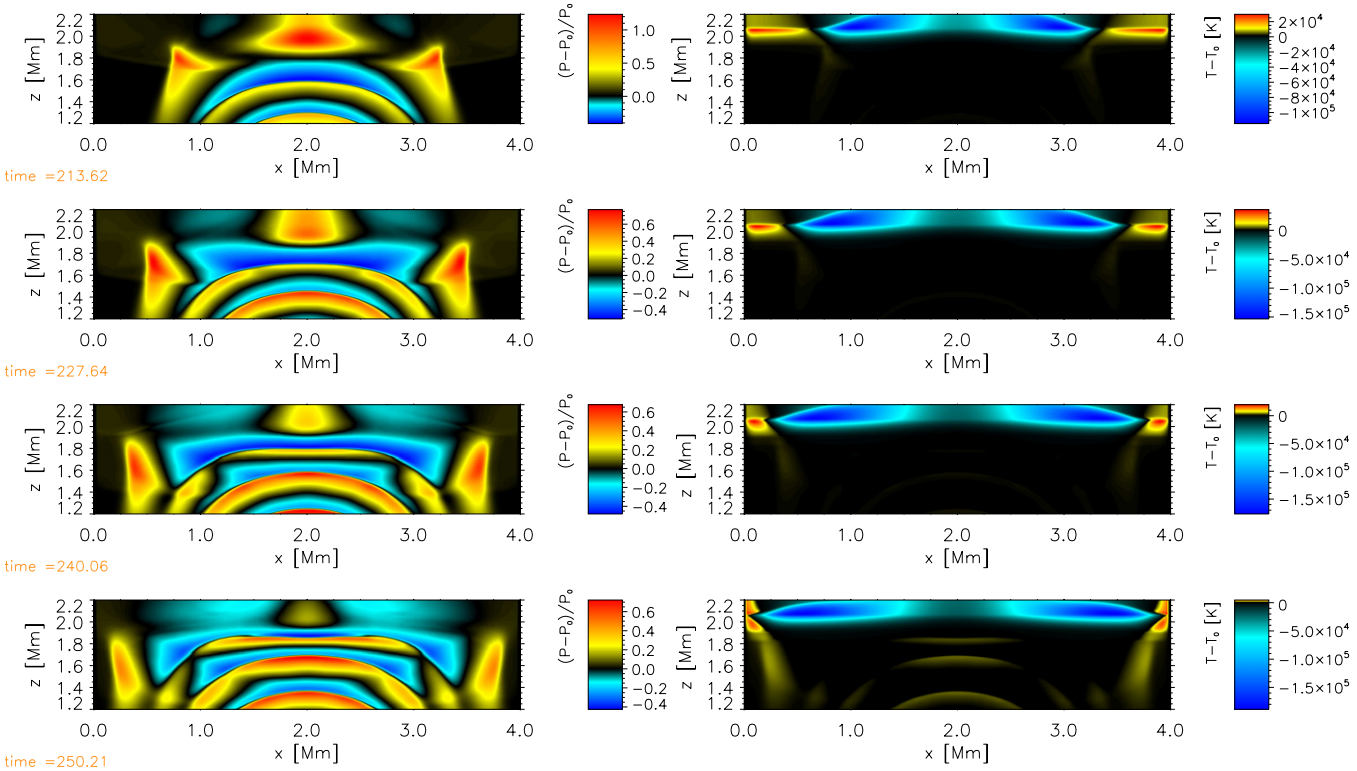

Figure 8. Time series of the relative pressure difference $\Delta P/P_0$ and temperature ΔT perturbation showing the development of a guided wave at the transition region from the vertical harmonic source. Only the zoomed out portion centered around the transition region is shown in the plots.

(A color version of this figure is available in the online journal.)

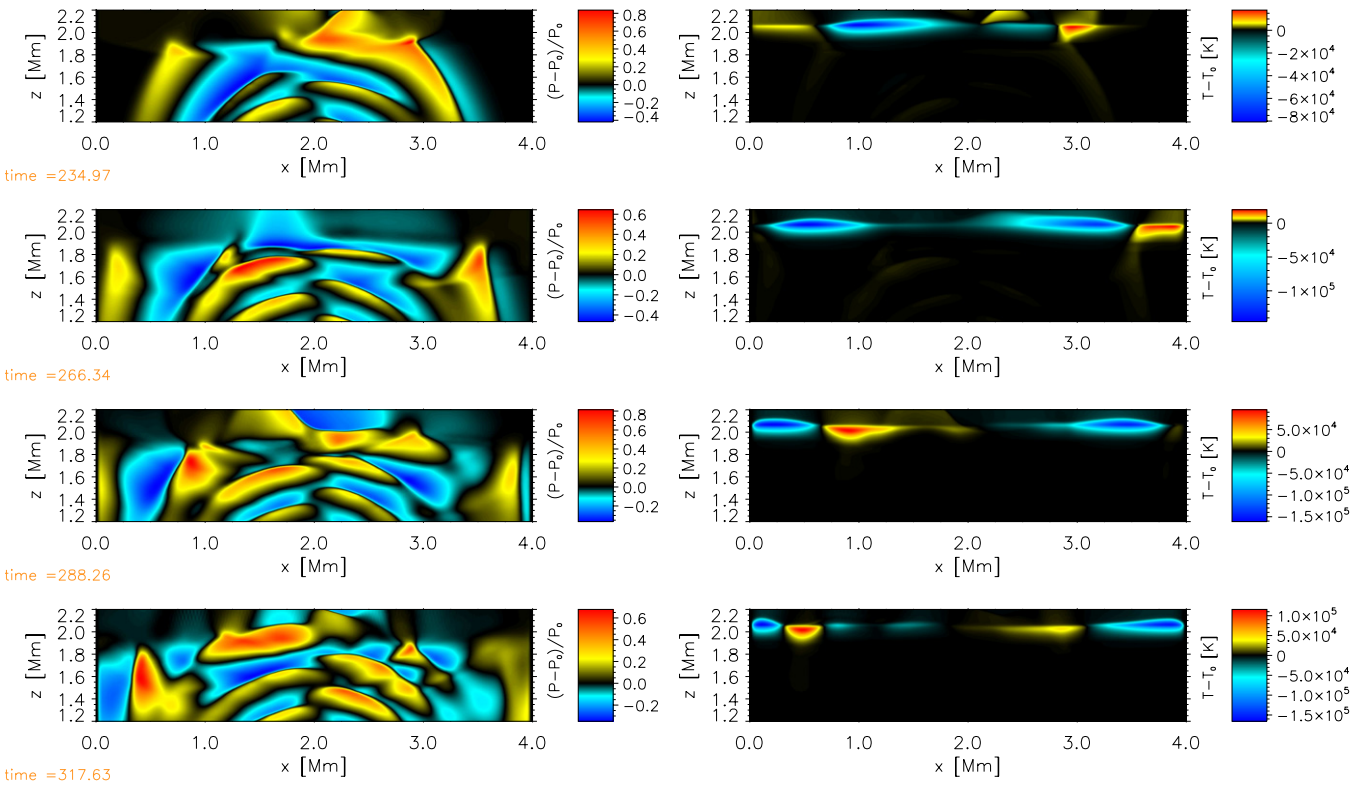

Figure 9. Same as Figure 8 but generated by the horizontal periodic driver (Equation (1)).

(A color version of this figure is available in the online journal.)

panels of Figure 10. These changes occur due to compression and rarefaction of the SMAW, as we have analyzed previously. There are no such variations in the perpendicular component of the velocity $V_\perp$ for either type of driver. The

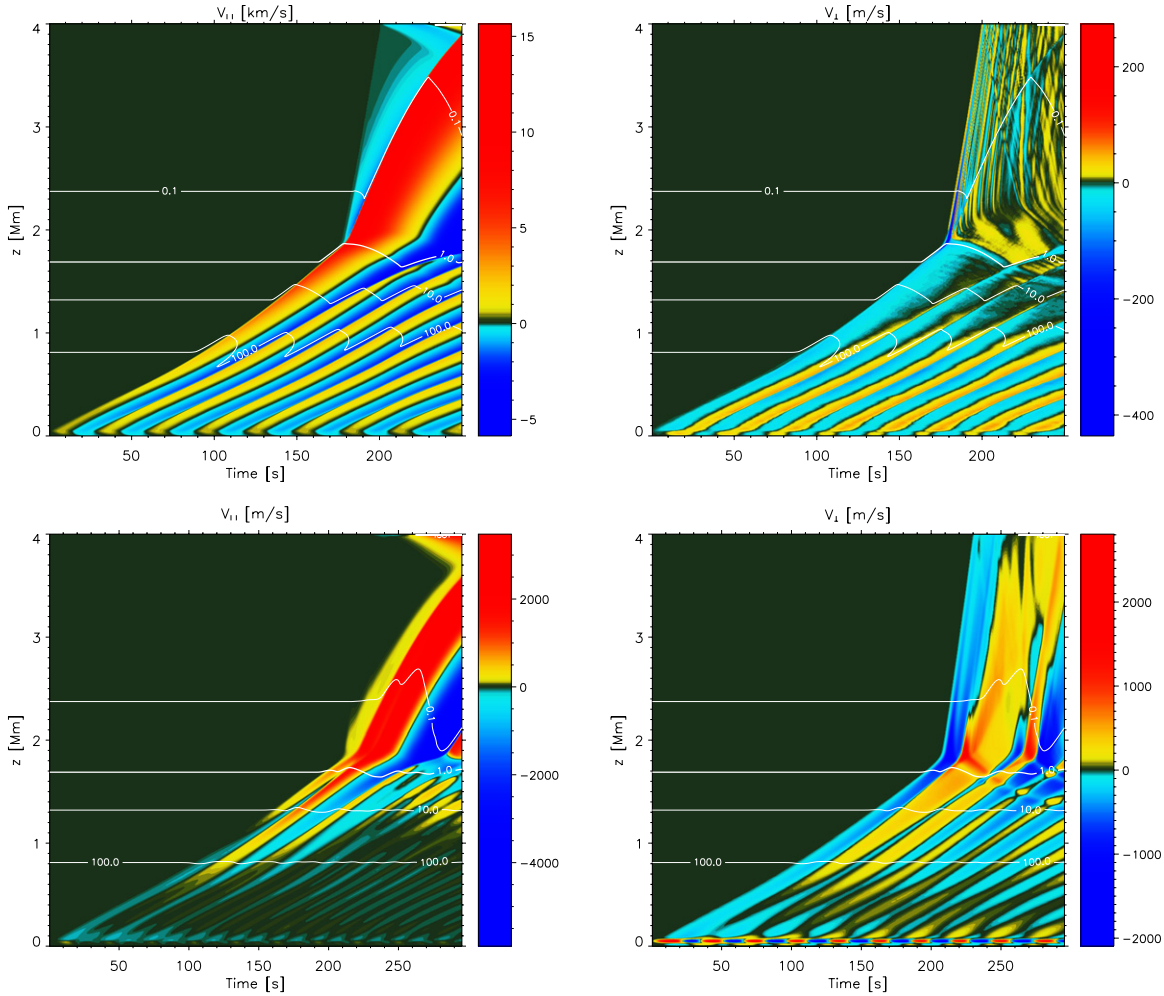

Figure 10. Altitude vs. time rendering of transverse ($V_\perp$) and field-aligned ($V_\parallel$) components of the velocity at $x = 2.0$ Mm, for vertical (upper panels) and transverse driving of perturbations. The white lines show the altitude variations of selected iso-plasma-β contours with time, labeled by their appropriate value.
(A color version of this figure is available in the online journal.)

steepening of the first SMAW, i.e., propagating speed, is faster than that of the following compression waves (see the two upper panels of Figure 10). No such behavior is observed for waves generated by the horizontal driver. The phase speeds and the amplitudes of slow and fast MAWs have increased after leaking into the corona region.

The propagation speed, i.e., phase speed of the wave associated with $V_\parallel$ and generated by a vertical driver, reaches a value equal to 26 km s^{-1} and has an amplitude 15 km s^{-1}. The waves associated with $V_\perp$ and generated by the same photospheric driver travels in the coronal region much faster, with velocities up to 100 km s^{-1}, but with a negligible value of amplitude, i.e., less than 0.5 km s^{-1} (along the axis of the tube). The phase speeds of the waves excited by the horizontal driver are the same as for the vertical driver due to their similar nature, but their amplitudes are different. In the coronal region the value of the $V_\parallel$ component increases up to 6.5 km s^{-1} and the value of $V_\perp$ up to 3 km s^{-1}. Wave reflection from the TR at $x = 2.0$ Mm is clearly visible on the time–distance diagrams in the $V_\parallel$ and $V_\perp$ components of the velocity for the horizontal driver.

Next, we construct the time–distance diagrams for both the $V_\parallel$ and $V_\perp$ velocity components in the horizontal direction at different heights of the solar atmosphere. The full movies of the phase speed variation with height, i.e., the evolution of the generated waves in the computational domain, are again available at the Web site http://swat.group.shef.ac.uk.

Figures 11 and 12 are the ω–k diagrams of the $V_\parallel$ and $V_\perp$ velocity components at representative heights 0.85 Mm and 1.5 Mm, respectively. The upper and lower panels of Figures 11 and 12 correspond to the wave spectrum generated in the computational domain by the vertical and horizontal drivers, respectively. The left and right panels in both figures correspond to the vertical ($V_\parallel$) and horizontal ($V_\perp$) components of the velocity. Figure 11 (i.e., the spectrum taken at 0.85 Mm) allows us to see and interpret clearly the signature of standing modes being set up within the chromospheric cavity (see Erdélyi et al. 2007) generated by both vertical (two upper panels) and horizontal (two lower panels) drivers.

For waves excited by a strongly localized driver (e.g., point source) this will produce single dots only in an ω–k diagrams that correspond to different harmonics of the standing mode. In our simulations we have used a velocity perturbation driver with Gaussian spatial profiles in the x and z directions (see Equation (1)). Such a source has a wide power spectrum, thus in our ω–k diagrams the standing modes appear as wider horizontal lines. The localized horizontal areas with the high signal power settle along a straight line, which is due to the approximately constant sound speed (see Figure 2) in the lower part of the

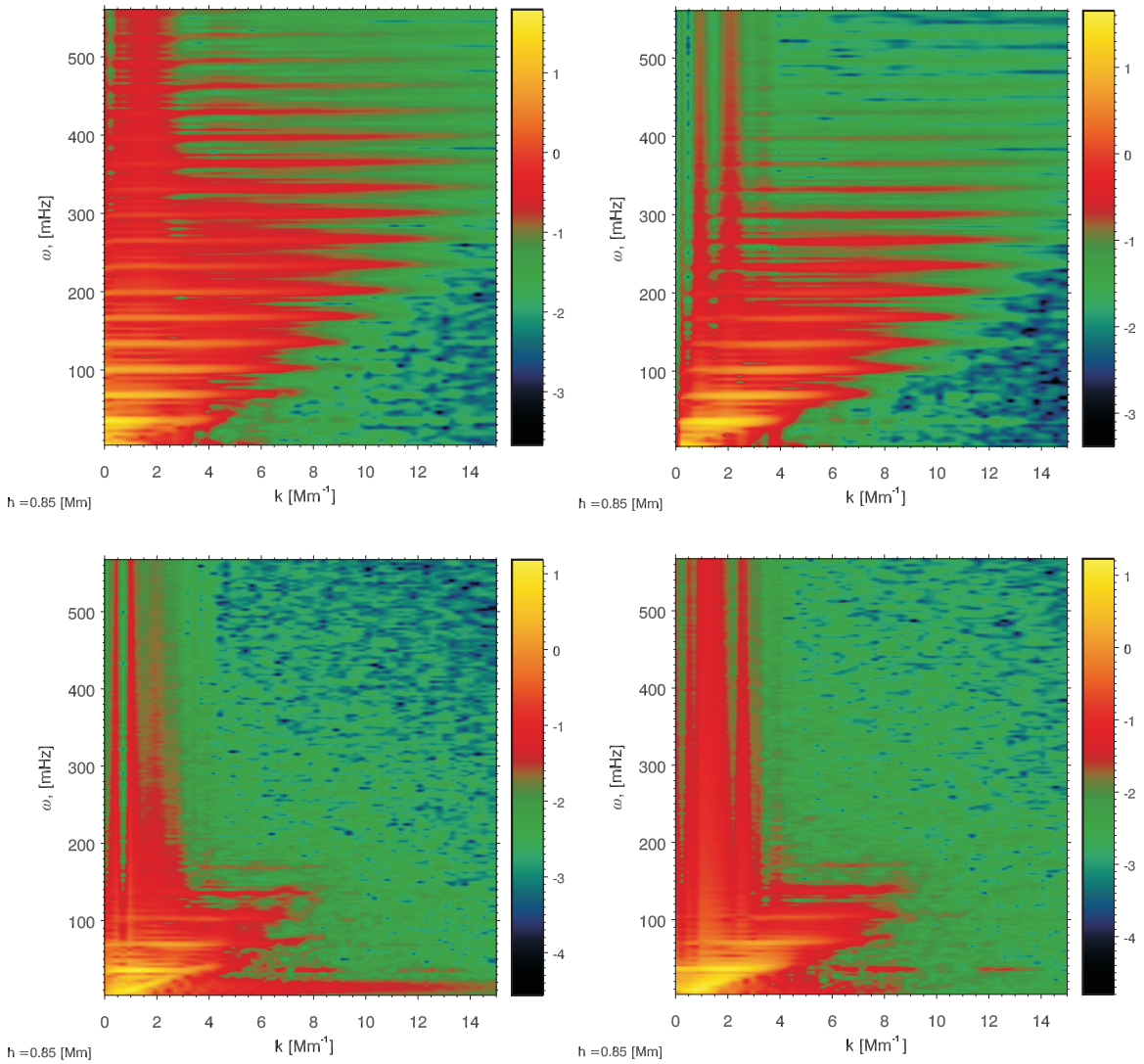

Figure 11. ω–k diagrams of the $V_{\parallel}$ and $V_{\perp}$ velocity components taken along the horizontal cross section at the chromosphere region, i.e., at 0.85 Mm in the vertical direction. The upper and lower panels correspond to the $V_{\parallel}$ and $V_{\perp}$ velocity components generated by the vertical and horizontal photospheric drivers defined by Equation (1), respectively.

(A color version of this figure is available in the online journal.)

computational domain in the horizontal direction along which the spectrum is calculated. The wave spectrum generated by vertical driver of ∼33.3 mHz contains evidence of the higher harmonics at ∼66.6, 100 mHz, and so on (see two upper panels of Figure 11). In the case of wave excitation by the horizontal driver (see the two lower panels of Figure 11) we can observe only four harmonics (at 33.3, ∼66.6, ∼100, and ∼133 mHz) at the chromospheric region. The area covered by higher harmonics of standing modes driven by the vertical driver is much larger than the corresponding area in the ω–k diagrams computed for the case of the horizontal driver. Therefore, we suggest that vertical motions are responsible for the formation of the standing mode pattern within the chromospheric cavity.

Figure 12 demonstrates the wave spectrum at the upper part of the chromosphere, i.e., at height equal to 1.5 Mm. In the central part of the flux tube, where the magnetic field is strong, the sound speed has a minimum value (see Figure 2). The plasma-β in this region is ∼10, therefore the magnetic flux tube starts to work as a cavity in a horizontal direction. Notably, at a height of 1.5 Mm the gradient of the signals corresponding to standing modes is increasing with wave number due to the influence of the cavity produced by the open flux tube (see Figure 12). Also, Figure 12 (see the left and the right lower parts) shows the presence of propagating slow and fast waves generated by the photospheric horizontal driver, which can be identified in the ω–k diagrams as two straight ridges. These ridges have a different inclination to the wave number axis k, so they correspond to waves propagating with different phase speeds. Only one ridge is observed at 1.5 Mm with the vertical driver (see the two upper panels of Figure 12).

Next, snapshots of the dispersion diagrams taken below the transition region (i.e., at heights $h = 1.8$ Mm and 1.85 Mm) and in the solar coronal region (i.e., at heights $h = 2.53$ and 3.03 Mm), are shown in Figures 13 and 14 are shown. In these parts of the computational domain magnetic field lines of the open flux tube (see Figure 3) are dominantly vertical. Thus, horizontal cross sections (which we have used to construct the time–distance and ω–k diagrams) are perpendicular to the magnetic field lines. In the lower part of the computational domain, the horizontal cross sections have various angles to the

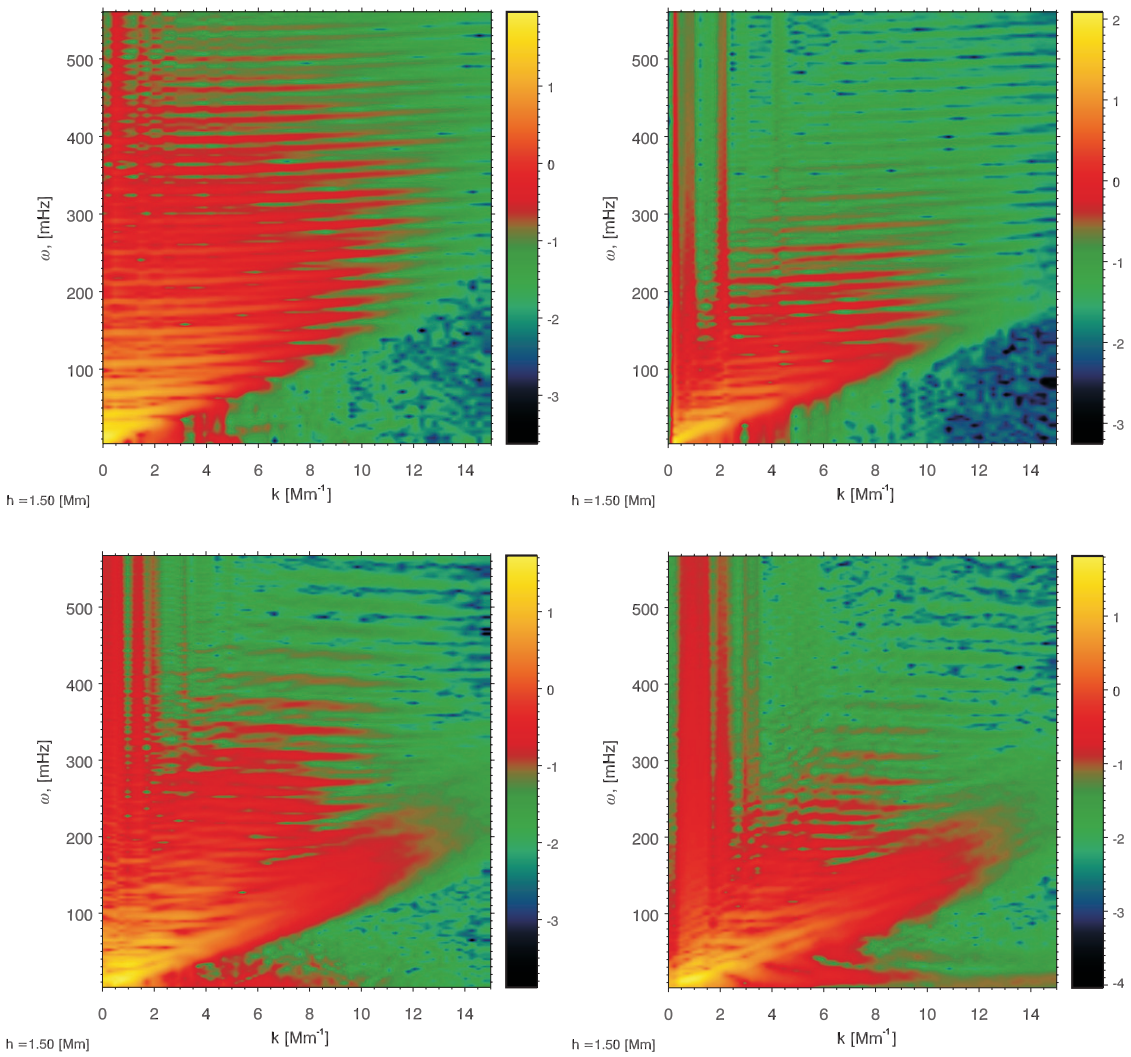

Figure 12. Same as Figure 11 but the velocity components are taken along the horizontal cross section at the vertical height 1.5 Mm.
(A color version of this figure is available in the online journal.)

magnetic field lines of the magnetic flux tube due to a curvature of the constructed magnetic field.

Because of this, interpretation of the ω–k diagrams where the magnetic field lines are not straight, i.e., in the photosphere and lower chromosphere regions, is not a straightforward task. In our simulations the region where the plasma-β is equal to unity is located just under the transition region, where the solar atmosphere has a steep temperature gradient. Figure 13 depicts the power spectrum and phase speeds of the waves generated by the photospheric vertical driver in this region. The four upper panels captured for the $V_{\parallel}$ velocity component while the four lower panels are plots of the $V_{\perp}$ velocity component. The presence of a number of ridges in this region can be explained from a magneto-seismological point of view. In our case, density in the region below the transition region and, thus the sound speed (see Figure 2), changes not only in the vertical z-direction (see Figure 1) but also in the horizontal x-direction. In Figure 13 we can clearly observe the signature of eigenmodes similar to the spectrum of solar acoustic oscillations. We suppose this ridge pattern was excited because the background model we use represents a cavity, bounded by the magnetic flux tube walls, in some way resembling a cavity, created by the upper and lower turning points in the solar interior.

Due to the wave reflection from the transition region and mode conversion within the plasma-$\beta \sim 1$ region, we can see propagating waves with different phase speeds (see the four left snapshots of Figure 13 for representative heights $h = 1.8$ Mm and 1.85 Mm). The process of mode conversion within the plasma-$\beta \sim 1$ region has been previously studied analytically and semi-analytically for non-realistic models by, e.g., Zhugzhda (1979), Cally (2001, 2007), and others. The enhanced power at certain frequencies is caused by partial reflections from the steep temperature and density profiles at the transition region in combination with the cavity. The pattern is observed in both the vertical (the upper four panels) and horizontal (the lower four panels) components of the velocity. As was mentioned previously, the energy carried by the horizontal component has its main impact on the guided waves in the transition region. Also, in the snapshot at $h = 1.86$ (see the second upper panel of Figure 13) the two types of ridges, indicated by the different gradients to the k-axis appear at the same location.

In the coronal region (see four snapshots in the right part of Figure 13 for the typical heights $h = 2.53$ Mm and 3.03 Mm), only one ridge is observed. The phase speed of the propagating wave is approximately constant and equal to $\sim$100 km s^{-1},

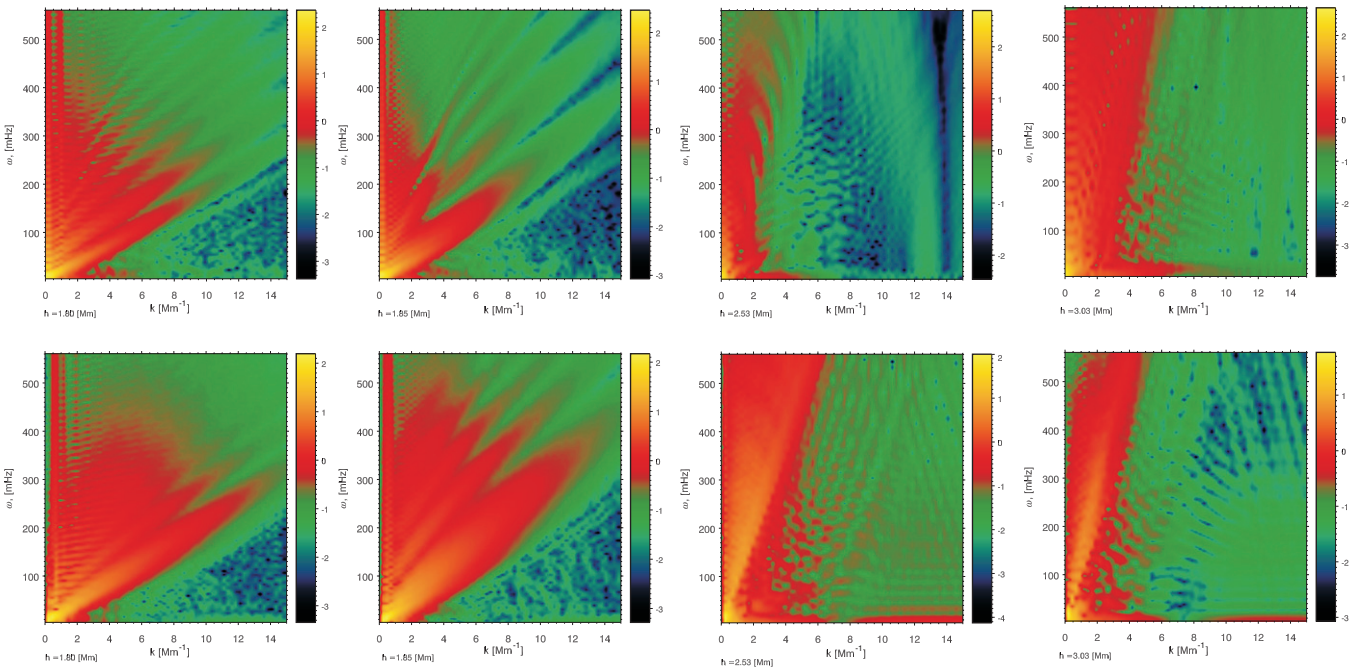

Figure 13. ω–k diagrams of the vertical $V_\parallel$ and horizontal $V_\perp$ velocity components in the transition and solar corona regions. Fourier transform performed on time–distance series are taken at heights $h = 1.8$, 1.85, 2.53, and 3.03 Mm. The four panels are the ω–k diagrams of $V_\parallel$ and $V_\perp$ velocity components excited by vertical photospheric driver (Equation (1)) in each row, respectively.

(A color version of this figure is available in the online journal.)

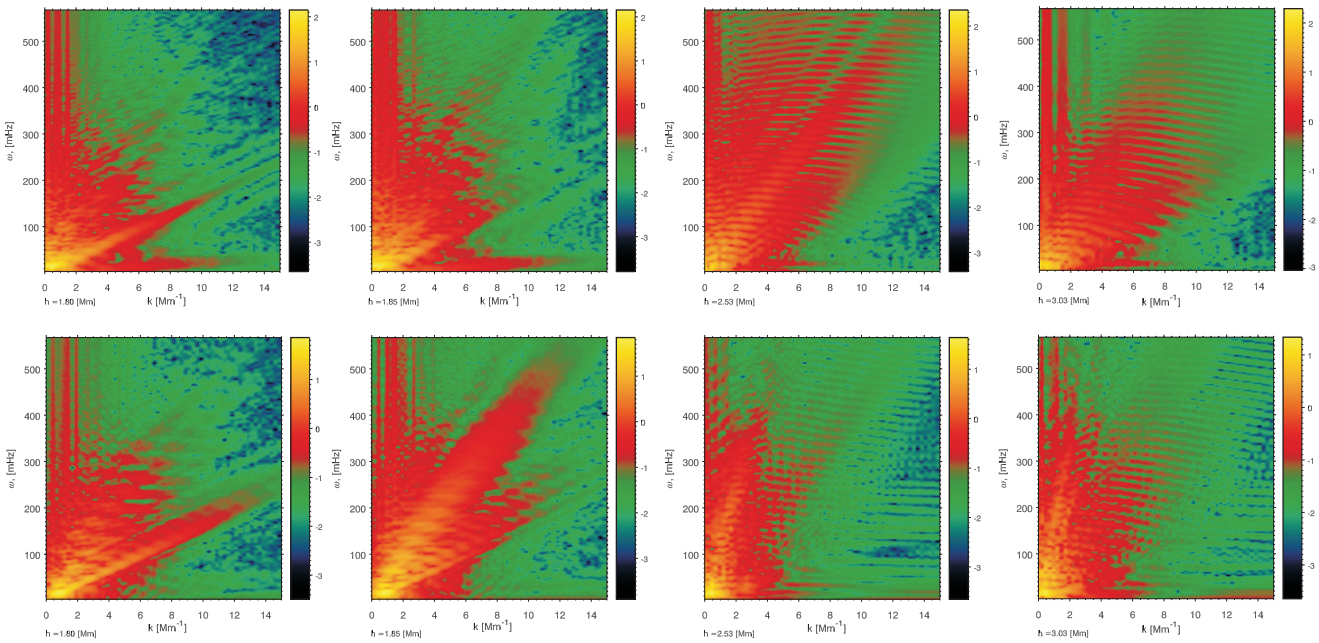

Figure 14. Same as Figure 13 but the $V_\parallel$ and $V_\perp$ velocity components are now generated by a horizontal photospheric driver.

(A color version of this figure is available in the online journal.)

slightly increasing with height. This is the same order of magnitude that has been observed with CoMP (see, e.g., Tomczyk & McIntosh 2009).

In Figure 14 we show a series ω–k diagrams taken at the same heights as the diagrams described above but for $V_\parallel$ and $V_\perp$ velocity components generated by a horizontal photospheric driver. Opposite to the previous case of wave generation by the vertical driver, the wave spectrum pattern within the transition region, excited by the horizontal driver, mainly keeps the structure of the wave spectrum in the upper chromosphere (see Figure 12). Thus, we can deduce that the vertical driver more strongly excites the eigenmodes near the transition region within the semi-circular shaped cavity.

5. CONCLUSIONS

In the present paper, we have made an attempt to numerically simulate wave generation and propagation in an open magnetic flux tube. It has been shown that standing modes within the chromospheric cavity are generated mainly by vertical motions

at the footpoint of an open magnetic flux tube. Regardless of the driver direction, the largest proportion of energy is carried to the corona via the $V_{\parallel}$ velocity component. It was also shown that the surface waves generated at the TR have most of their power in the perpendicular velocity component $V_{\perp}$, irrespective of whether the driver is horizontal or vertical. Hence, the oscillatory response of the flux tube at the TR and above in the corona is weakly dependent on whether the velocity of the driver is parallel or perpendicular to the direction of the magnetic field at the footpoint. These facts have important implications for high spatial and temporal observations of lower atmospheric flux tubes by, e.g., *Hinode*, ROSA, and the planned ATST, suggesting that the oscillatory response of such flux tubes should be similarly independent of photospheric driver, e.g., the previously mentioned TR surface waves and dominant vertical velocity component power.

Unfortunately, we cannot yet compare our results directly with the time–distance and FFT analysis of the CoMP observational data (Tomczyk & McIntosh 2009) for a number of reasons. Firstly, the spatial resolution of CoMP is 9 arcsec, which is about 6.5 Mm. In our simulations we have used a numerical domain of 4 Mm × 4 Mm, thus CoMP cannot resolve the fine spatial structure generated in our model. Second, the S/N of the CoMP instrument decreases with frequency and at the frequency above 5 mHz the level of noise is comparable with the signal, and in our case the frequency is well above this range. In our paper, we have analyzed the dependence of ω and the perpendicular wavenumber whereas Tomczyk & McIntosh (2009) estimated the wavenumber parallel to observing magnetic field. However, it is possible to carry out such a study with our present data and this will be the subject of future work. Future work will also include non-adiabatic effects, such as radiative losses from coronal shocks, and a detailed non-ideal equation of state. Another possibility would be to reduce the spatial resolution of our numerical domain and, thus, increase the physical size of the solar atmospheric model. Either way, the present paper is a step toward the wider interpretation of CoMP (and other coronal wave) observations and we hope giving here impetus to design further such important parallel to observing campaigns.

The authors thank The University of Sheffield (UK), Queen's University Belfast (UK), and STFC (UK) for the financial support they received. R.E. acknowledges M. Kéray for patient encouragement and is grateful to NSF, Hungary (OTKA, Ref. No. K67746).

REFERENCES

Andries, J., van Doorsselaere, T., Roberts, B., Verth, G., Verwichte, E., & Erdélyi, R. 2009, Space Sci. Rev., 149, 3
Banerjee, D., Erdélyi, R., Oliver, R., & O'Shea, E. 2007, Sol. Phys., 246, 3
Bogdan, T. J., et al. 2003, ApJ, 599, 626
Cally, P. S. 2001, ApJ, 548, 473
Cally, P. S. 2007, Astron. Nachr., 328, 286
Cargill, P. J., Spicer, D. S., & Zalesak, S. T. 1997, ApJ, 488, 854
Carlsson, M., & Bogdan, T. J. 2006, Phil. Trans. R. Soc. A, 364, 395
Caunt, S. E., & Korpi, M. J. 2001, A&A, 369, 706
Deinzer, W. 1965, ApJ, 141, 548
De Moortel, I. 2009, Space Sci. Rev., 149, 65
De Pontieu, B., & Erdélyi, R. 2006, Phil. Trans. R. Soc. A, 364, 383
De Pontieu, B., Erdélyi, R., & De Moortel, I. 2005, ApJ, 624, L61
De Pontieu, B., Erdélyi, R., & James, S. P. 2004, Nature, 430, 536
Díaz, A. J., & Roberts, B. 2006, A&A, 458, 975
Dorotovič, I., Erdélyi, R., & Karlovský, V. 2008, in IAU Symp. 247, Identification of Linear Slow Sausage Waves in Magnetic Pores, ed. R. Erdélyi & C. A. Mendoza-Briceño (Cambridge: Cambridge Univ. Press), 351
Erdélyi, R. 2006, Phil. Trans. R. Soc. A, 364, 351
Erdélyi, R., & Fedun, V. 2007, Science, 318, 1572
Erdélyi, R., Malins, C., Tóth, G., & De Pontieu, B. 2007, A&A, 467, 1299
Erdélyi, R., & Taroyan, Y. 2008, A&A, 489, L49
Fedun, V., Erdélyi, R., & Shelyag, S. 2009, Sol. Phys., 258, 219
Fossum, A., & Carlsson, M. 2005, Nature, 435, 919
Goedbloed, J. P. H., & Poedts, S. 2004, Principles of Magnetohydrodynamics (Cambridge: Cambridge Univ. Press)
Goossens, M., Terradas, J., Andries, J., Arregui, I., & Ballester, J. L. 2009, A&A, 503, 213
Gordovskyy, M., & Jain, R. 2007, ApJ, 661, 586
Hasan, S. S., & van Ballegooijen, A. A. 2008, ApJ, 680, 1542
Hasan, S. S., van Ballegooijen, A. A., Kalkofen, W., & Steiner, O. 2005, ApJ, 631, 1270
Keppens, R., Nool, M., Tóth, G., & Goedbloed, J. P. 2003, Comput. Phys. Commun., 153, 317
Khomenko, E., & Collados, M. 2006, ApJ, 653, 739
Khomenko, E., Collados, M., & Felipe, T. 2008, Sol. Phys., 251, 589
Kuridze, D., Zaqarashvili, T. V., Shergelashvili, B. M., & Poedts, S. 2009, A&A, 505, 763
Mathioudakis, M., Jess, D. B., & Erdélyi, R. 2011, Space Sci. Rev., submitted
McWhirter, R., Thonemann, P., & Wilson, R. 1975, A&A, 40, 63
Musielak, Z. E., Rosner, R., Stein, R. F., & Ulmschneider, P. 1994, ApJ, 423, 474
Ofman, L. 2009, Space Sci. Rev., 149, 153
Ruderman, M. S., & Erdélyi, R. 2009, Space Sci. Rev., 149, 199
Ruderman, M. S., Verth, G., & Erdélyi, R. 2008, ApJ, 686, 694
Schunker, H., & Cally, P. S. 2006, MNRAS, 372, 551
Schüssler, M., & Rempel, M. 2005, A&A, 441, 337
Schlüter, A., & Temesváry, S. 1958, in IAU Symp. 6, Electromagnetic Phenomena in Cosmical Physics, ed. B. Lehnert (Cambridge: Cambridge Univ. Press), 263
Scullion, E., Erdélyi, R., Fedun, V., & Doyle, J. 2010, ApJ, submitted
Shelyag, S., Fedun, V., & Erdélyi, R. 2008, A&A, 486, 655
Shelyag, S., Mathioudakis, M., Keenan, F. P., & Jess, D. B. 2010, A&A, 515, A107
Shelyag, S., Zharkov, S., Fedun, V., Erdélyi, R., & Thompson, M. J. 2009, A&A, 501, 735
Stein, R. F., & Nordlund, A. 1998, ApJ, 499, 914
Taroyan, Y., & Erdélyi, R. 2009, Space Sci. Rev., 149, 229
Tomczyk, S., & McIntosh, S. W. 2009, ApJ, 697, 1384
Tóth, G. 1996, Astrophys. Lett. Commun., 34, 245
Tóth, G. 2000, J. Comput. Phys., 161, 605
Tóth, G., Keppens, R., & Botchev, M. A. 1998, A&A, 332, 1159
Vernazza, J. E., Avrett, E. H., & Loeser, R. 1981, ApJS, 45, 635
Verth, G., & Erdélyi, R. 2008, A&A, 486, 1015
Verth, G., Erdélyi, R., & Goossens, M. 2010, ApJ, 714, 1637
Verth, G., Erdélyi, R., & Jess, D. B. 2008, ApJ, 687, L45
Vögler, A., Shelyag, S., Schüssler, M., Cattaneo, F., Emonet, T., & Linde, T. 2005, A&A, 429, 335
Zaqarashvili, T. V., & Skhirtladze, N. 2008, ApJ, 683, L91
Zhugzhda, Y. D. 1979, SvA, 23, 42